Chemosphere 197 (2018) 65–72

Contents lists available at ScienceDirect

Chemosphere

journal homepage: www.elsevier.com/locate/chemosphere

Combined effects of Ag and UiO-66 for removal of elemental mercury from flue gas

Songjian Zhao [a, b], Dongyao chen [a], Haomiao Xu [a], Jian mei [a], Zan Qu [a], Ping Liu [a], Yong Cui [b], Naiqiang Yan [a, *]

[a] School of Environmental Science and Engineering, Shanghai Jiao Tong University, 800 Dong Chuan Road, Shanghai, 200240, PR China
[b] School of Chemistry and Chemical Engineering, Shanghai Jiao Tong University, 800 Dong Chuan Road, Shanghai, 200240, PR China

HIGHLIGHTS

- Ag nanoparticles were introduced into UiO-66 for Hg^0 removal.
- Ag and UiO-66 presented a synergistic effect.
- The temperature window of UiO-66-Ag was wide.

GRAPHICAL ABSTRACT

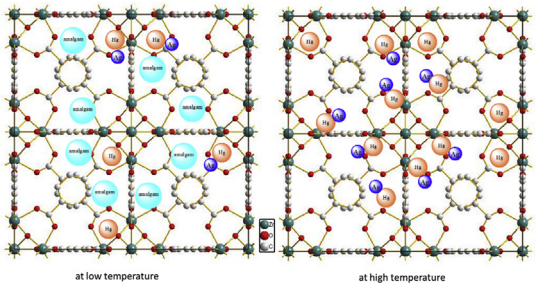

ARTICLE INFO

Article history:
Received 22 June 2017
Received in revised form
2 October 2017
Accepted 6 January 2018
Available online 9 January 2018

Handling Editor: Min Jang

Keywords:
Ag nanoparticles
UiO-66
Mercury
Removal

ABSTRACT

The zirconium metal-organic framework material UiO-66 was doped with Ag nanoparticles and investigated for the removal of elemental mercury (Hg^0) in flue gas. Physical and chemical characterization of the adsorbents showed that adding Ag did not change the crystal structure and morphology of the UiO-66. Ag doping can improve the redox activity of UiO-66, and the adsorbent exhibited high thermal stability and surface area. Hg^0 removal experiments indicated that UiO-66 exhibited the higher performance compared with P25 and activated carbon, and the addition of Ag exhibited a significant synergistic effect with the UiO-66, which had highest Hg^0 adsorption capacity (3.7 mg/g) at 50 °C. Furthermore, the Hg^0 removal mechanism was investigated, revealing that Hg^0 is removed by the formation of an Ag amalgam and channel adsorption at low temperature, and through Ag-activated oxygen oxidation and channel capture at high temperature.

1. Introduction

Environmental pollution with mercury has attracted increasing attention in recent years because of its volatility, persistence, bioaccumulation, and neurological toxicity. Coal combustion is considered to be one of the major anthropogenic mercury sources due to the huge global consumption of coal (Yuan et al., 2012). Most of the mercury in coal is associated with pyrite, and other forms of mercury are organically bound, elemental, and in sulfide and selenide minerals (Gao et al., 2013). During combustion, mercury is released into the exhaust gas as elemental mercury vapor, which may then be oxidized via homogeneous and heterogeneous reactions. Therefore, mercury species emitted from coal-fired flue gas

* Corresponding author.
E-mail address: nqyan@sjtu.edu.cn (N. Yan).

https://doi.org/10.1016/j.chemosphere.2018.01.025
0045-6535/

are present in three forms: elemental mercury (Hg^0), oxidized elemental mercury (Hg^{2+}), and particle-bound elemental mercury (Hg^p). Generally speaking, Hg^{2+} and Hg^p are relatively easy to remove from flue gas using typical air pollution control methods, such as wet-flue gas desulfurization (wet-FGD) and electrostatic precipitators (ESPs)(Zhao et al., 2017). However, Hg^0 is the main mercury component of flue gas (Liu et al., 2011), and is difficult to remove owing to its high volatility and low solubility in water. Furthermore, all Hg species including Hg^0 can transform into highly toxic methylmercury, which can enter the food chain where it poses a serious threat to human health. Therefore, removal of Hg^0 from coal-fired flue gas is a very important issue.

Adsorption and oxidation are considered the two main methods for Hg^0 removal. Many adsorbents and catalysts for Hg^0 removal have been proposed in recent years, such as active carbon, selective catalytic reduction (SCR) catalysts, metal oxides, and noble metals (Abad-Valle et al., 2011; Li et al., 2011; Wdowin et al., 2014). Morency et al. reported the treated zeolite sorbent can effectively remove mercury from flue gases, and had similar capture rate with activated carbon (Morency, 2002). Malgorzata et al. prepared manganese oxides supported on zirconium dioxide for Hg^0 removal, and found the rate of Hg^0 capture on the particle surface area is dependent on manganese content and distribution (Wiatros-Motyka et al., 2013). However, few of them show any clear merit in either conversion efficiency or economy.

Metal-organic frameworks (MOFs) are an emerging class of porous materials comprised of different organic linkers and metal ions that have attracted widespread attention because of their ordered crystalline structures, controllable porosities, large internal surface areas, and countless structural topologies (Xu et al., 2015). Given these unique features, MOFs have motivated research for wide-ranging applications such as in gas storage and separation, drug delivery, and heterogeneous catalysis (Kim et al., 2011). MOFs can also be applied in Hg^0 removal because of their high surface areas and high volume fractions of active metal (Shahat et al., 2013).

However, weak thermal stability is a major disadvantage of MOFs. The zirconium MOF (UiO-66) is recently synthesized and shows high chemical and thermal stability. Consequently, several investigations into its functionalization and application in catalysis have been reported (Cao et al., 2014). In recent years, there have been several reports on Zr(IV)-based MOFs for Hg^0 removal. Zhang et al. synthesized phenyl bromine-appended MOFs and applied them to high-efficiency Hg^0 removal from simulated flue gas (Xiao et al., 2016). Saleem et al. investigated post-synthetically NH_2-modified UiO-66 for the adsorptive removal of heavy metal ions including Hg^{2+} from aqueous solution, and showed that $-NH_2$ functionalization markedly improved its metal removal efficiency (Saleem et al., 2016). Thus, UiO-66 could become a highly desirable and promising material or support for Hg^0 removal.

As a unique feature, Hg atoms can dissolve certain metal atoms to form amalgams, and amalgams decompose to release mercury to the gas phase at higher temperatures (Luglie et al., 2005). Given this feature, Ag has been widely studied as an adsorbent in Hg^0 removal due to its efficiency and low cost (Liu et al., 2008; Yuan et al., 2012). Furthermore, Ag can enhance the oxidizing ability of some metallic oxides for Hg^0 removal (Zhao et al., 2014). However, Ag atoms tend to coalesce into oligomers, which themselves progressively grow into larger clusters and eventually precipitate during preparation and calcination. Thus, it is necessary to seek a suitable carrier with large surface areas to provide highly dispersed Ag nanoparticles.

In this study, Ag and UiO-66 were combined to form an adsorbent for the removal of Hg^0 from flue gas. The physical and chemical properties of the adsorbents, as well as their Hg^0 removal efficiencies, were investigated. In addition, the mechanism involved in Hg^0 removal was discussed.

2. Experimental section

2.1. Materials

All chemicals used for adsorbent preparation were of analytical grade. Zirconium tetrachloride ($ZrCl_4$, >99%), 1,4-benzenedicarboxylic acid (H_2BDC, 99%), and N,N'-dimethylformamide (DMF, 99.5%) were purchased from Aladdin Co. (Shanghai, China); glacial acetic acid (CH_3COOH, >99.5%) and silver nitrate ($AgNO_3$, >99.8%) were purchased from Shanghai Ling Feng Chemical Reagent Co., Ltd. (Shanghai, China). Sodium borohydride ($NaBH_4$, 96%) was purchased from Sinopharm Chemical Reagent Co., Ltd.

2.2. Preparation of adsorbents

The synthesis of UiO-66 was performed using a modified procedure as described in the literature (Cao et al., 2014). Standard synthesis of UiO-66 was performed by dissolving $ZrCl_4$ (0.53 g, 2.27 mmol) and H_2BDC (0.35 g, 2.11 mmol) in DMF (100 mL) at room temperature. Acetic acid (3.5 mL) was then added to the mixture. The obtained mixture was sealed and placed in a preheated oven at 120 °C for 24 h. Crystallization was carried out under static conditions. After the solution was cooled to room temperature in air, the resulting solid was filtered and washed with DMF three times, and finally dried at 150 °C in an oven for 24 h. An amount of UiO-66 was dissolved in the solution of $AgNO_3$, and the molar ratio of Ag and Zr was 0.05. Then the solution of $NaBH_4$ (0.1 mol/L) was slowly added to the Ag and UiO-66 solution, which was finally dried at 150 °C in an oven for 24 h. The prepared adsorbent was labeled UiO-66-Ag. Because the activated carbon and P25 was a commonly used adsorbent/catalyst carrier, adding silver onto activated carbon and P25 were selected for performance comparison, marked as: C—Ag and P25—Ag.

2.3. Removal activity evaluation

The removal activity was evaluated in accordance with the previously described criteria (Zhao et al., 2015), including a simulative gas formulating system and reaction device (SHKD-1, Tongsheng Lida Digital Technology Co., Ltd., Beijing), a cold vapor atomic absorption spectrometer (CVAAS), and an online data acquisition system, shown in Fig. 1. The reaction system included eight mass flow controllers to adjust the simulated flue gas compositions and a fixed-bed reactor. The adsorbent was packed into the quartz tube, which was plugged with quartz wool. An Hg^0 permeation tube was used to generate Hg^0 vapor carried by pure N_2, which was then introduced to the inlet of the gas mixer. A cold vapor atomic absorption spectroscopy (CVAAS) analyzer was employed as an online continuous detector that could only detect Hg^0. The concentration of Hg^0 was measured using Lumex RA 915+. At the beginning of each test, the gas containing Hg^0 was first passed through a bypass without adsorbents to determine the baseline. When the concentration of Hg^0 had fluctuated within ±5% for more than 30 min, the gas was diverted to pass through the fixed-bed reactor containing the adsorbents. The amount of adsorbents were 20 mg and the gas flow rate was 500 mL min^{-1}, corresponding to a space velocity (SV) of 2.13×10^5 h^{-1}, using N_2 as carrier gas, and the O_2 content was 4%. The concentration of Hg^0 was approximately 250 $\mu g/m^3$.

The Hg^0 removal efficiency and adsorption capacities were calculated according to Eqs. (1) and (2):

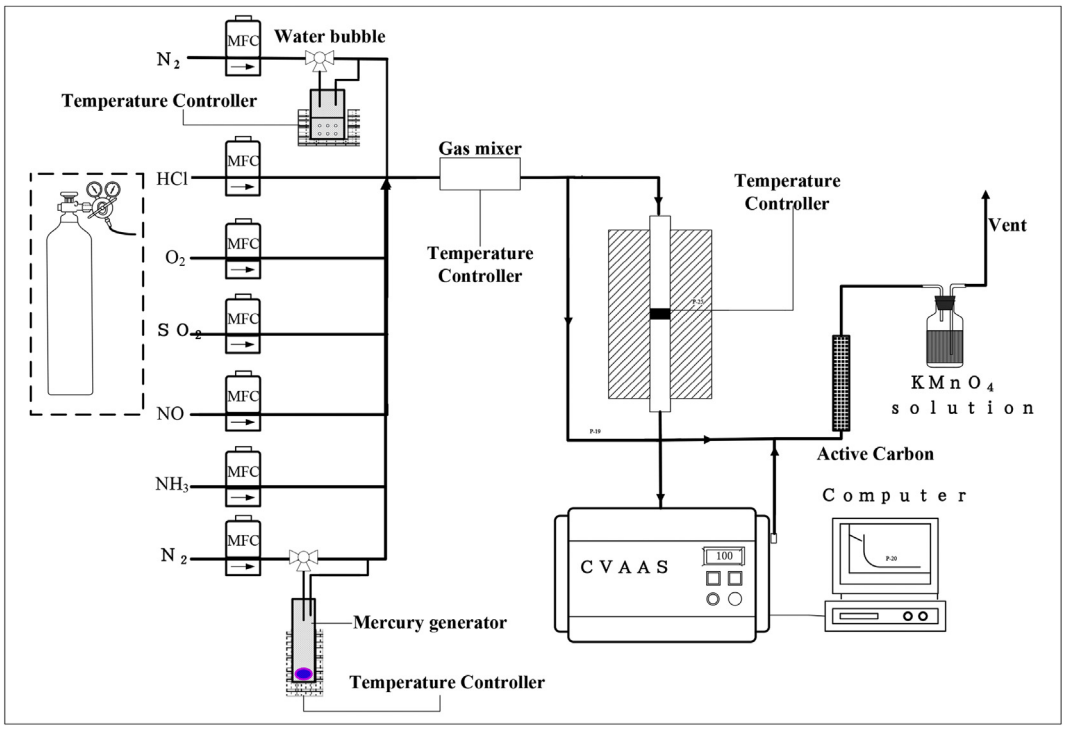

Fig. 1. Process flow diagram for Hg^0 removal performance assessment.

$$\eta = \frac{Hg^0_{in} - Hg^0_{out}}{Hg^0_{in}} \quad (1)$$

$$Q = \frac{1}{m}\int_{t2}^{t1}\left(\frac{Hg^0_{in} - Hg^0_{out}}{Hg^0_{in}}\right) \times f \times dt \quad (2)$$

where η is the Hg^0 removal efficiency, Hg^0_{in} is the inlet concentration of Hg^0, Hg^0_{out} is the outlet concentration of Hg^0, Q is the Hg^0 adsorption capacity, m is the mass of the adsorbent in the fixed-bed, f is the flow rate of the influent, and t_1 and t_2 are the initial and final test times, respectively.

The temperature programmed desorption (TPD) curves of Hg were obtained as follows: A known amount of adsorbents were placed in a reaction device with N_2 + 4% O_2 at 500 mL min^{-1} to adsorb Hg^0 for 30 min. Then, the oxygen flow was stopped, and the Hg signal curve was recorded under N_2. The heating rate was 5 °C min^{-1}, and the temperature range was from 20 °C to 600 °C.

The valence state change for Hg was analyzed using a Tekran 3300 RS online mercury emissions monitoring system. The analytical method employed was cold atomic fluorescence and enrichment of pure gold amalgam.

2.4. Characterization of the adsorbents

The prepared adsorbents were characterized and analyzed using different techniques. The microstructure of the adsorbents was analyzed by transmission electron microscopy (TEM), and the samples were dispersed in ethanol with strong sonication before analysis. The X-ray diffraction (XRD) patterns of the adsorbents were obtained using an APLX-DUO X-ray diffractometer (BRUKER, Germany) using Cu Kα radiation (40 kV and 20 mA), and the XRD patterns were recorded in a 2θ range from 5 to 70° at a scanning rate of 5°min^{-1}. The thermal stabilities of the adsorbents were assessed using a TGA/DSC1 (Mettler Toledo), and the ramp rate for the thermogravimetric analysis (TGA) was 10 °C min^{-1} from 30 to 700 °C. Nitrogen adsorption and desorption isotherms were obtained on a nitrogen-adsorption apparatus (Quantachrome Nova 2200e) at −196 °C. All samples were degassed first for 3 h at 200 °C. Specific surface areas were calculated by use of the Brunauer-Emmett-Teller (BET) method. H_2-temperature programmed reduction (H_2-TPR) experiments were performed on a Chemisorp TPx 2920 instrument, the sorbents were degassed at 200 °C for 3 h under Ar at atmosphere before H_2-TPR test, and the reducing gas was 10% H_2/Ar. X-ray photoelectron spectroscopy (XPS) measurements were made using an AXIS UltraDLD (Shimadzu-Kratos) spectrometer with Al Kα radiation as the excitation source. The C1s line at 284.8 eV was taken as a reference for binding energy calibration.

3. Results and discussion

3.1. Physical and chemical characterization

To study the morphologies of the prepared adsorbents, TEM analysis was performed, and the resulting images are shown in Fig. 2 (a). UiO-66 presents cubic particles and exhibits intact crystal morphology. The UiO-66 particles are approximately 200 nm in size, and no impurities are found on their surfaces. When Ag is introduced, many small particles attached to the surfaces of the UiO-66 are observed, which could be Ag nanoparticles. The size of these particles is approximately 20 nm, and they are well dispersed on the surface of the UiO-66. In addition, the morphology of the UiO-66-Ag remains cubic, indicating that the addition of Ag does not change the crystal form of UiO-66.

Fig. 2 (b) shows the XRD patterns of UiO-66 and UiO-66-Ag. The UiO-66 sample presents sharp peaks that match those reports for UiO-66 (Xu et al., 2015; Dong et al., 2016), indicating that the UiO-

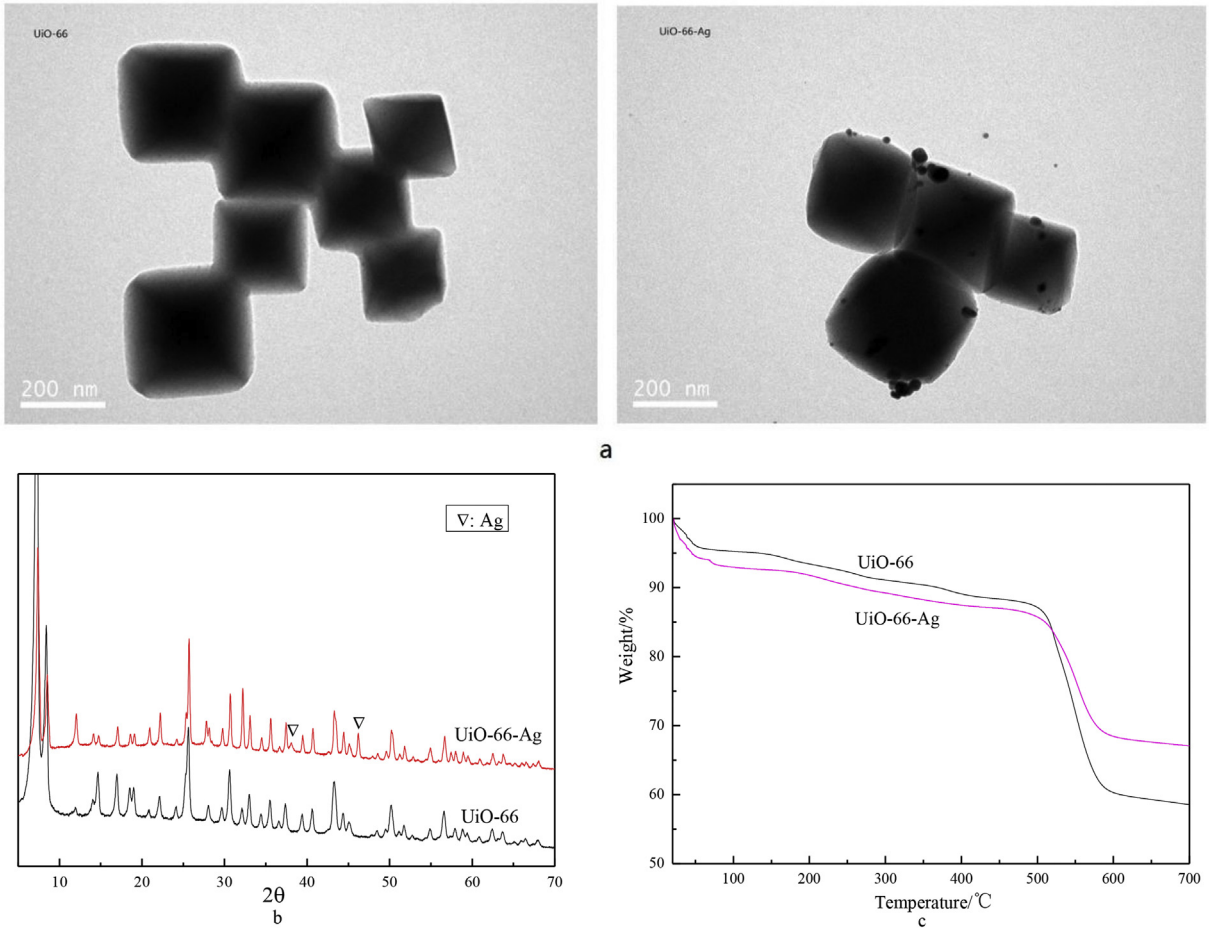

Fig. 2. Physical and chemical characterization of UiO-66 and UiO-66-Ag: The transmission electron microscopy (a), XRD patterns (b) and the TG curves.

66 adsorbent was successfully prepared with excellent crystallinity. The diffraction peaks for UiO-66-Ag are similar to those for UiO-66, indicating that UiO-66 undergoes no loss of crystallinity upon Ag coordination and maintains its crystal structure. In addition, there are two additional diffraction peaks (marked ◇), which can be readily indexed as the (111) and (200) planes of metallic Ag (JCPDS No. 04-0783), confirming the successful application of metallic Ag (Zhang et al., 2012).

To confirm the stability and structural integrity of UiO-66 and UiO-66-Ag at elevated temperatures the samples were subjected to TGA, the results of which are shown in Fig. 2 (c). UiO-66 and UiO-66-Ag present similar TG curves. At the very beginning, a weights loss by the adsorbents is observed below 100 °C, which can be attributed to physically adsorbed water, guest water, and solvent molecules. After that, there is very little weight loss for UiO-66 and UiO-66-Ag until approximately 500 °C, indicating that UiO-66 and UiO-66-Ag have high thermal stability and can be used for removing Hg^0 at high temperature. A sharp weight loss is observed beyond 500 °C, indicating the structural collapse of the adsorbents, which is in good agreement with reported studies (Cao et al., 2014). The weight loss for UiO-66 is approximately 7.4% from 100 to 500 °C, which may be due to the loss of residual organic matter. There is a weight loss of approximately 33% from 500 to 700 °C for UiO-66, which might be due to the loss of the organic framework. For UiO-66-Ag, the weight loss is approximately 8% from 100 to 500 °C, and approximately 20.5% from 500 to 700 °C, which are less than that for UiO-66 due to the residual Ag. On the whole, the added Ag has little effect on the thermal stability of UiO-66.

The TPR profiles for UiO-66 and UiO-66-Ag are shown in Fig. S1. There is one apparent reduction peak starting from 500 °C with a maximum at 600 °C in Fig. S1 (a) that can be attributed to the reduction of zirconium oxides, which might be because the skeletal structure of UiO-66 is damaged. After adding Ag, there is an additional peak located at about 220 °C, which can be ascribed to highly dispersed Ag_2O and cationic Ag clusters (Ag_n^+) (Góramarek et al., 2015). The peak for the reduction of zirconium oxides in UiO-66-Ag is lower than that in UiO-66, indicating that the added Ag promotes the reduction of zirconium oxides and the mobility of lattice oxygen species, which is beneficial for the process of Hg^0 oxidation (Góramarek et al., 2015).

The N_2 adsorption-desorption isotherms of UiO-66 and UiO-66-Ag are shown in Fig. S2. The specific surface areas and pore volumes of the adsorbents were calculated from these isotherms and are listed in Table S1. The N_2 adsorption-desorption isotherm for all the adsorbents are assigned as type IV with hysteresis loops at high relative pressure. UiO-66 presents a large BET surface area and pore volume, which is beneficial for loading metal particles and adsorbing reaction components. Even though the BET surface area of UiO-66-Ag is smaller than that of UiO-66, it still presents a larger surface area. Furthermore, the smaller pore volume indicates that some Ag nanoparticles are loaded into the UiO-66 channels in UiO-66-Ag.

Fig. 3 shows the XPS spectra of UiO-66-Ag over the Zr 3d, O 1s, Ag 3d and Hg 4f spectral regions. The binding energies of the Zr

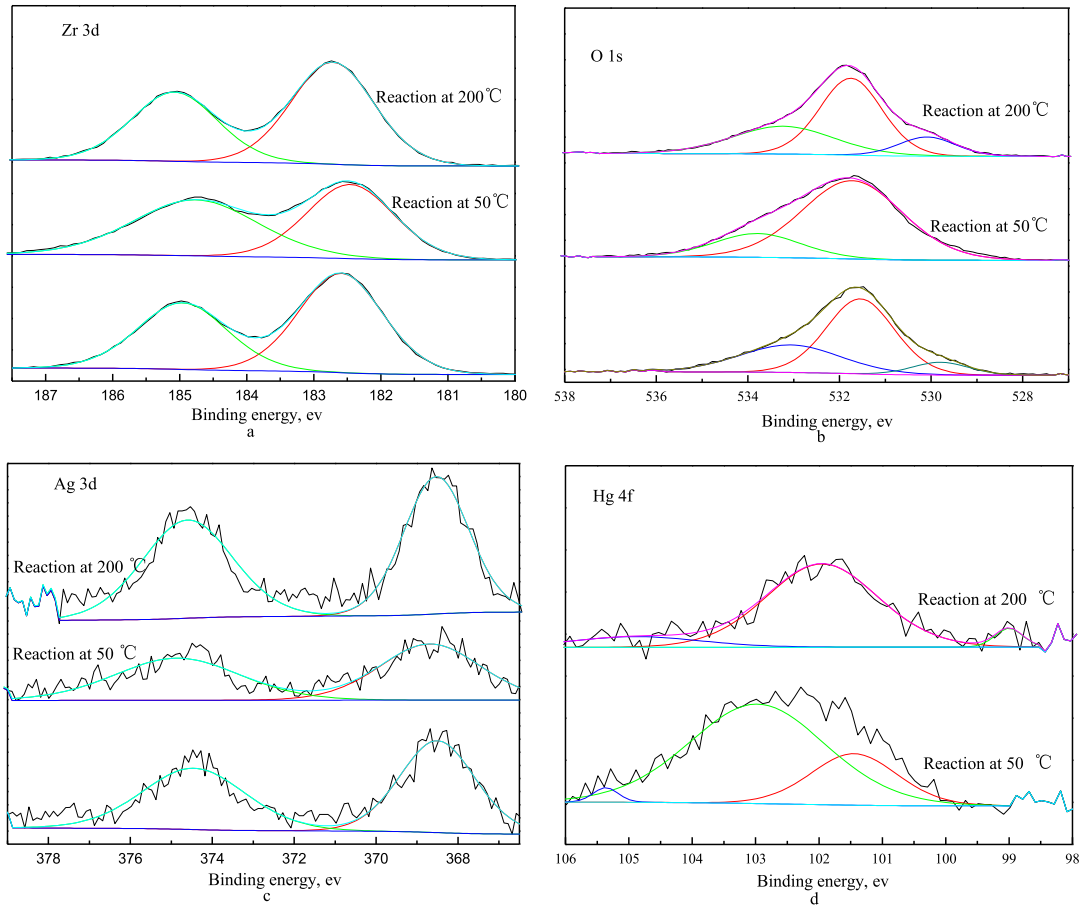

Fig. 3. The XPS spectra of UiO-66-Ag over the spectral regions: Zr 3d (a), O 1s (b), Ag 3d (c) and Hg 4f (d).

3d5/2 and Zr 3d3/2 peaks located at around 182.5 and 185 eV can be attributed to zirconium in the Zr^{4+} state. This indicates that Zr exists as ZrO_2 in the tetragonal phase (Barrera et al., 2012). After reaction at 50 °C, the intensity of the Zr 3d peaks is weaker, which might be due to some Hg^0 adsorbed onto the surface of the adsorbent. And it can be found that the position of the Zr 3d peak shifts slightly to a higher binding energy upon reaction at 200 °C, which might because of the combination effect with Hg^0.

The O 1s XPS spectrum of UiO-66-Ag is shown in Fig. 3 (b) and can be deconvoluted into three peaks. The peak at 529.8 eV can be ascribed to lattice oxygen due to Zr–O bonds, and the peak at 531.4 eV can be attributed to weakly surface chemisorbed oxygen. The peak at approximately 533.2 eV can be attributed to oxygen components of the carboxylate groups (O–C=O) (Zhang et al., 2011) due to the unreactive ligand. Compared with the O 1s XPS spectrum of UiO-66 (shown in Fig. S3), it is clear that the peak for chemisorbed oxygen is more intense, and that the peak for O–C=O oxygen is less obviously, which might be that the added Ag promotes the transformation of O–C=O oxygen species into active oxygen. It has been reported that the C=O bond in the form of carboxyl or ester groups can improve Hg^0 chemical adsorption capacity (Tan et al., 2012), and Ag can generate electrophilic oxygen (Delaigle et al., 2011), so the added Ag can significantly enhance Hg^0 removal capacity by activating C=O.

It is difficult to detect lattice oxygen after the reaction at 50 °C, indicating that the generated Ag amalgam is adsorbed onto the surface of the adsorbent and weakens the signal for the Zr–O bonds. However, the proportion of lattice oxygen increases after reaction at 200 °C, which might be due to the effect of generated Hg–O. Furthermore, the proportion of surface chemisorbed oxygen decreases, indicating that the chemisorbed oxygen participates in the process of Hg^0 oxidation.

The Ag 3d XPS peaks were investigated in this work, and are shown in Fig. 3 (c). It has been reported that the peaks at 367.90 and 373.94 eV can be attributed to Ag(I), and those at 368.23 and 374.09 eV can be attributed to Ag (0) (Zhao et al., 2015). It can be seen clearly that Ag is mostly present in the metallic state, which indicates that the particles on the UiO-66, first detected in the TEM experiments, are Ag nanoparticles. Ag can combine with Hg^0 to form an Ag amalgam at low temperature, leading to the reduced characteristic Ag 3d peak intensity at 50 °C. However, upon reaction at 200 °C, the intensity and position of the Ag 3d peak does not change, indicating Ag does not combine with Hg at this temperature.

Fig. 3 (d) shows the Hg 4f XPS patterns. It was reported that the Hg 4f 7/2 binding energy at 99.9 eV was attributed to Hg^0. As can be found in Fig. 3 (d), the peak position of Hg 4f was higher than that of Hg^0, indicated that the reaction product adsorbed on the adsorbent was not Hg^0. After reaction at 50 °C, the spectrum of Hg 4f could be divided into two peaks, the binding energy at about 101.5 ev might correspond Hg alloy due to the generated silver amalgam (Ramasindarum et al., 2012), while the higher binding energy at 103 eV may be attributed to Si due to the use of silica wool (Li et al., 2015). After reaction at 200 °C, the binding energy at about 101.8 eV can be attributed to Hg^{2+}, indicated that Hg^0 is oxidized over UiO-66-Ag.

3.2. The analysis of Hg^0 removal

Fig. 4 (a) shows Hg^0 removal efficiencies of various adsorbents at 10 h under different temperatures. Because the activated carbon and P25 was a commonly used adsorbent/catalyst carrier, which were selected for Hg^0 removal comparison with UiO-66. P25 presents poor Hg^0 removal efficiency, after adding Ag nanoparticles, the adsorbent activity of adsorbent has less increase. Activated carbon shows some adsorption capacity, While the increase of C–Ag performance still little. UiO-66 exhibits the highest performance compared with P25 and activated carbon, and the Hg^0 removal efficiency observably increased after adding Ag, indicating that UiO-66 is a better support for Hg^0 removal, and that the uniformly dispersed Ag nanoparticles exhibit a significant synergistic effect with the UiO-66.

UiO-66-Ag exhibits high Hg^0 removal ability at 50 and 200 °C. The high Hg^0 removal efficiency at 50 °C might be due to the formation of an Ag amalgam. With increasing temperature, the Hg^0 concentration first decreases and subsequently increases up to 200 °C, which might be due to the fact that the formed Ag amalgam decomposes and the oxidation ability of the adsorbent increases. However, the Hg^0 removal efficiency decreases slightly at 250 °C. This might be because Hg^0 adsorption is poor at high temperature. Generally, efficient Hg^0 removal occurs through the synergy of adsorption and oxidation.

UiO-66 presents a similar trend for Hg^0 removal to that of UiO-66-Ag. This indicates that UiO-66 also has moderate Hg^0 removal activity due to channel capture and oxidation of C=O. Ag is important for the improvement of Hg^0 removal activity at different temperatures.

Fig. 4 (b) shows the Hg^0 adsorption capacity over UiO-66-Ag at different temperatures. The results indicate that UiO-66-Ag has high adsorption capacity, and can be applied over a wide temperature range.

Fig. S4 shows the Hg^0 breakthrough curves over UiO-66-Ag under 4% oxygen and 0% oxygen at 50 and 200 °C. The Hg^0 removal efficiency is still high at 0% oxygen, indicating that oxygen has little effect on Hg^0 removal. The removal mechanism at low temperature mainly involves physical adsorption, while at high temperature it mainly involves chemical adsorption based on the oxygen species the adsorbent presents, such as the oxygen components of the carboxylate groups.

The effect of HCl and H_2O for Hg^0 removal efficiency was studied in Fig. S5. It found that the effect of HCl was little, and water inhibited the Hg^0 removal. Furthermore, the repeat ability of UiO-66-Ag was good, and the Hg^0 removal efficiency can still reach above 85% after using spent adsorbent for four times (Fig. S6).

3.3. The analysis of Hg^0 desorption

Hg^0 adsorption and desorption experiments were performed to study the Hg combination properties of the adsorbents, as shown in Fig. 5. Fig. 5 (a) shows the Hg-temperature programmed desorption (Hg-TPD) curves for UiO-66 and UiO-66-Ag after adsorption for 30 min at 50 °C. It can be seen from Fig. 5 (a) that there is no Hg^0 desorption until 500 °C for UiO-66, which indicates that Hg^0 is not adsorbed onto its surface. According to the TG curve for UiO-66, the desorbed Hg^0 is due to the structural collapse of the adsorbent, whereupon the Hg^0 adsorbed in the UiO-66 channels is released as a gas. There are two desorption peaks for UiO-66-Ag. The peak starting at 100 °C and ending at approximately 200 °C is attributed to the release of Ag amalgam. The other peak with the maximum at 500 °C may be due to the decomposition of the adsorbent structure. The desorption amount is more than that for UiO-66, maybe because some Ag nanoparticles are located in the UiO-66 channels. Hg^0 begins to be released slowly from 250 °C, which might be due to the release of chemically adsorbed Hg.

Fig. 5 (b) shows the Hg-TPD curves for UiO-66 and UiO-66-Ag after adsorption for 30 min at 200 °C. It can be seen that Hg^0 desorbs from UiO-66 above 200 °C, which might be the Hg^{2+} generated by C=O oxidation (*cf.* the XPS results). The sharp peak at approximately 500 °C is attributed to structural collapse. Three desorption peaks are clearly presented for UiO-66-Ag. The peak starting from 100 °C might be due to Hg^0 adsorbed in the channels of the sample, and the peak starting from 250 °C and ending at approximately 350 °C can be assigned to the chemical adsorption of Hg on the surface of the adsorbent. The peak starting from 350 °C is attributed to the physical and chemical adsorption of Hg inside the channels of the adsorbent. Owing to the effect of the Ag, the amount of Hg released is more than that for UiO-66.

3.4. The valence state change analysis of the mercury

To further confirm the above results and speculations, the valence state variation for mercury was analyzed. Fig. 6 shows the Hg valence state curves at 50 °C and 200 °C. The difference in the value for total mercury (Hg^t) and elemental mercury (Hg^0) is the amount of divalent mercury (Hg^{2+}). It can be seen from Fig. 6 that the concentrations of Hg^t and Hg^0 both decrease when the flue gas passes through the adsorbent. And the concentrations and the difference value for Hg^t and Hg^0 are constantly low at 50 °C and 200 °C, indicating that there is little mercury species in the gas, and

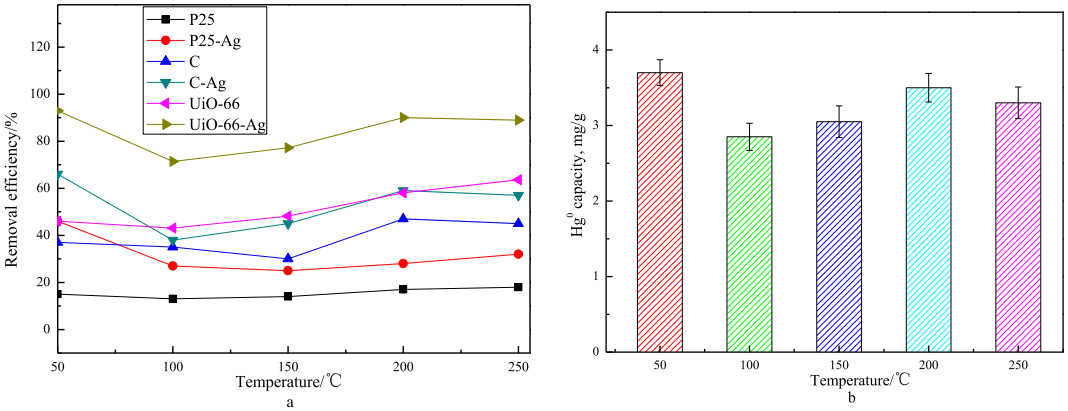

Fig. 4. Hg^0 removal efficiencies of the adsorbents at 10 h at different temperatures (a), Hg^0 adsorption capacity over UiO-66-Ag at different temperatures (b), the concentration of Hg^0 was approximately 250 μg/m^3.

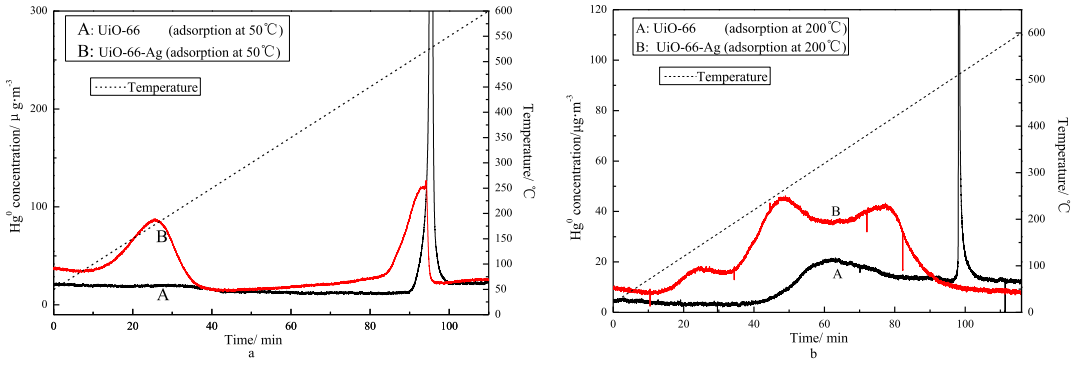

Fig. 5. The Hg-TPD curves for adsorbents.

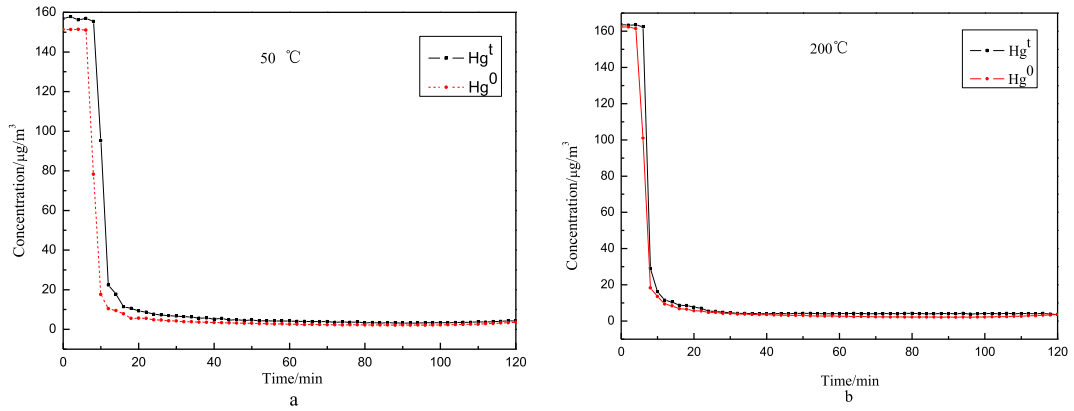

Fig. 6. The mercury valence state curves at 50 and 200 °C.

that the mercury mainly exists on the adsorbent. Based on the XPS results and the mercury concentration change curves, it can be speculated that mercury is adsorbed on the adsorbent presenting Ag amalgam at low temperature and Hg^{2+} at high temperature.

3.5. The main reaction pathway

Based on these results, a plausible mechanism for Hg^0 removal has been proposed as follows (Fig. 7):

At low temperature, Hg^0 is mainly removed by forming an Ag amalgam and through channel adsorption. At high temperature, Ag transfers an electron to the C═O oxygen species of unreactive carboxyl or ester groups, generating active oxygen, which then abstracts an electron from Hg^0 through Ag. Furthermore, the generated active zirconium also combines with Hg^0, presented in the form of a compound. Hg^0 can also be adsorbed and then captured in the channels of UiO-66 at high temperature.

4. Conclusions

In summary, Ag nanoparticles were introduced into UiO-66, exhibiting high Hg^0 removal efficiency. The addition of Ag did not change the original topology of and crystal structure the adsorbent framework. UiO-66-Ag composite showed improved redox ability, and high thermal stability and specific surface area. UiO-66 presented higher performance compared with P25 and activated

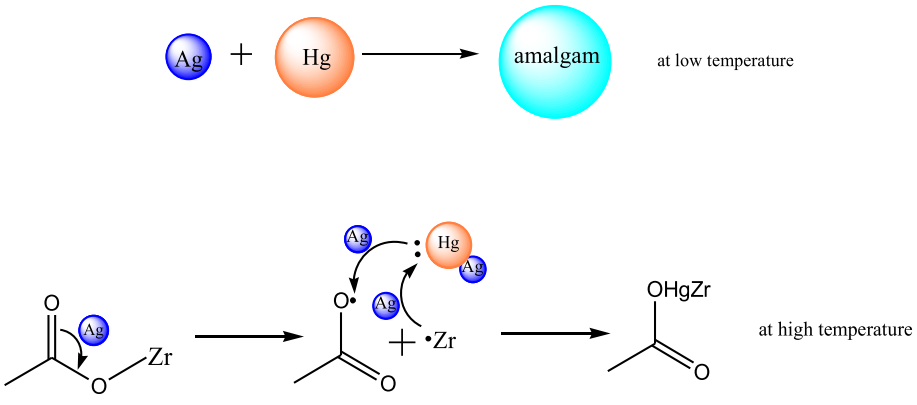

Fig. 7. The reaction process for the Hg^0 oxidation.

carbon, and Ag exhibited a significant synergistic effect with the UiO-66. Besides, UiO-66-Ag has good repeat ability and a wide windows for Hg^0 removal. Hg^0 can be removed by the formation of an Ag amalgam and channel adsorption at low temperature, And Hg^0 was removed through Ag-activated oxygen oxidation and channel capture at high temperature.

Acknowledgements

This study was supported by the National Key Research and Development Program of China (No. 2017YFC0210502) and the National Natural Science Foundation of China (No. 21677096) and (No.21607102), and China's Post-doctoral Science Fun (No. 2015M581626).

Appendix A. Supplementary data

Supplementary data related to this article can be found at https://doi.org/10.1016/j.chemosphere.2018.01.025.

References

Abad-Valle, P., Lopez-Anton, M.A., Diaz-Somoano, M., Martinez-Tarazona, M.R., 2011. The role of unburned carbon concentrates from fly ashes in the oxidation and retention of mercury. Chem. Eng. J. 174, 86–92.

Barrera, A., Montoya, J.A., Angel, P.D., Navarrete, J., Cano, M.E., Tzompantzi, F., López-Gaona, A., 2012. Surface properties of palladium catalysts supported on ternary ZrO_2 –Al_2O_3 –WOx oxides prepared by the sol–gel method: study of the chemical state of the support. J. Phys. Chem. Solid. 73, 1017–1025.

Cao, Y., Zhao, Y., Lv, Z., Song, F., Zhong, Q., 2014. Preparation and enhanced CO_2 adsorption capacity of UiO-66/graphene oxide composites. J. Ind. Eng. Chem. 27, 102–107.

Delaigle, R., Eloy, P., Gaigneaux, E.M., 2011. Necessary conditions for a synergy between Ag and V_2O_5 in the total oxidation of chlorobenzene. Catal. Today.

Dong, W., Feng, C., Li, Z., Shang, N., Gao, S., Wang, C., Wang, Z., 2016. Pd@UiO-66: an efficient catalyst for suzuki–miyaura coupling reaction at mild condition. Catal. Lett. 146, 1–9.

Góramarek, K., Tarach, K.A., Piwowarska, Z., Łaniecki, M., Chmielarz, L., 2015. Ag-loaded zeolites Y and USY as catalysts for selective ammonia oxidation. Catal. Sci. Technol. 6, 1651–1660.

Gao, Y.S., Zhang, Z., Wu, J.W., Duan, L.H., Umar, A., Sun, L.Y., Guo, Z.H., Wang, Q., 2013. A critical review on the heterogeneous catalytic oxidation of elemental mercury in flue gases. Environ. Sci. Technol. 47, 10813–10823.

Kim, M., Cahill, J.F., Prather, K.A., Cohen, S.M., 2011. Postsynthetic modification at orthogonal reactive sites on mixed, bifunctional metal-organic frameworks. Chem. Commun. 47, 7629–7631.

Li, G., Shen, B., Li, Y., Zhao, B., Wang, F., He, C., Wang, Y., Zhang, M., 2015. Removal of element mercury by medicine residue derived biochars in presence of various gas compositions. J. Hazard Mater. 298, 162–169.

Li, H., Wu, C.Y., Li, Y., Zhang, J., 2011. CeO_2 –TiO_2 catalysts for catalytic oxidation of elemental mercury in low-rank coal combustion flue gas. Environ. Sci. Technol. 45, 7394–7400.

Liu, Y., Kelly, D.J.A., Yang, H., Lin, C.C.H., Kuznicki, S.M., Xu, Z., 2008. Novel regenerable sorbent for mercury capture from flue gases of coal-fired power plant. Environ. Sci. Technol. 42, 6205–6210.

Liu, Y., Wang, Y., Wang, H., Wu, Z., 2011. Catalytic oxidation of gas-phase mercury over Co/TiO_2 catalysts prepared by sol–gel method. Catal. Commun. 12, 1291–1294.

Luglie, P.F., Campus, G., Chessa, G., Spano, G., Capobianco, G., Fadda, G.M., Dessole, S., 2005. Effect of amalgam fillings on the mercury concentration in human amniotic fluid. Arch. Gynecol. Obstet. 271, 138–142.

Morency, J.R., 2002. Zeolite sorbent that effectively removes mercury from flue gases. Filtrat. Separ. 39, 24–26.

Ramasindarum, C., Balakrishnan, V., Kasim, N.H.A., Yarmo, M.A., 2012. Structural and Compositional Characterization of Silverfil Amalgam. Springer Berlin Heidelberg.

Saleem, H., Rafique, U., Davies, R.P., 2016. Investigations on post-synthetically modified UiO-66-NH_2 for the adsorptive removal of heavy metal ions from aqueous solution. Microporous Mesoporous Mater. 221, 238–244.

Shahat, A., Hassan, H.M., Azzazy, H.M., 2013. Optical metal-organic framework sensor for selective discrimination of some toxic metal ions in water. Anal. Chim. Acta 793, 90–98.

Tan, Z., Sun, L., Xiang, J., Zeng, H., Liu, Z., Hu, S., Qiu, J., 2012. Gas-phase elemental mercury removal by novel carbon-based sorbents. Carbon 50, 362–371.

Wdowin, M., Wiatros-Motyka, M.M., Panek, R., Stevens, L.A., Franus, W., Snape, C.E., 2014. Experimental study of mercury removal from exhaust gases. Fuel 128, 451–457.

Wiatros-Motyka, M.M., Sun, C.G., Stevens, L.A., Snape, C.E., 2013. High capacity co-precipitated manganese oxides sorbents for oxidative mercury capture. Fuel 109, 559–562.

Xiao, Z., Shen, B., Xu, H., Tian, L., 2016. UiO-66 and its Br-modified derivates for elemental mercury removal. J. Hazard Mater. 320, 556–563.

Xu, Z., Xu, C.L., Yang, L., 2015. Pt@UiO-66 heterostructures for highly selective detection of H2O2 with an extended linear range. Anal. Chem. 87, 3438–3444.

Yuan, Y., Zhao, Y., Li, H., Li, Y., Gao, X., Zheng, C., Zhang, J., 2012. Electrospun metal oxide–TiO_2 nanofibers for elemental mercury removal from flue gas. J. Hazard Mater. 227–228, 427–435.

Zhang, H., Huang, H., Ming, H., Li, H., Zhang, L., Liu, Y., Kang, Z., 2012. Carbon quantum dots/Ag_3PO_4 complex photocatalysts with enhanced photocatalytic activity and stability under visible light. J. Mater. Chem. 22, 10501–10506.

Zhang, P., Shao, C., Zhang, Z., Zhang, M., Mu, J., Guo, Z., Liu, Y., 2011. In situ assembly of well-dispersed Ag nanoparticles (AgNPs) on electrospun carbon nanofibers (CNFs) for catalytic reduction of 4-nitrophenol. Nanoscale 3, 3357–3363.

Zhao, S., Ma, Y., Qu, Z., Yan, N., Li, Z., Xie, J., Chen, W., 2014. The performance of Ag doped V_2O_5 -TiO_2 catalyst on the catalytic oxidation of gaseous elemental mercury. Catal. Sci. Tech. 4, 4036–4044.

Zhao, S., Qu, Z., Yan, N., Li, Z., Zhu, W., Pan, J., Xu, J., Li, M., 2015. Ag-modified AgI–TiO_2 as an excellent and durable catalyst for catalytic oxidation of elemental mercury. Rsc Adv. 5, 30841–30850.

Zhao, S.J., Xu, H.M., Mei, J., Ma, Y.P., Lou, T., Qu, Z., Yan, N.Q., 2017. Ag-Mo modified SCR catalyst for a co-beneficial oxidation of elemental mercury at wide temperature range. Fuel 200, 236–243.